Eur. Phys. J. D (2013)
DOI: 10.1140/epjd/e2013-40276-1

THE EUROPEAN PHYSICAL JOURNAL D

Colloquium

Modelling low energy electron and positron tracks in biologically relevant media

Francisco Blanco[1], Antonio Muñoz[2], Diogo Almeida[3], Filipe Ferreira da Silva[3], Paulo Limão-Vieira[3], Martina C. Fuss[4], and Ana G. Sanz[4], Gustavo García[4,5,a]

[1] Departamento de Física Atómica, Molecular y Nuclear, Universidad Complutense de Madrid, 28040 Madrid, Spain
[2] Centro de Investigaciones Energéticas Medioambientales y Tecnológicas, Avenida Complutense 22, 28040 Madrid, Spain
[3] Laboratório de Colisões Atómicas e Moleculares, CEFITEC, Departamento de Física, Faculdade de Ciências e Tecnologia, Universidade Nova de Lisboa, 2829-516 Caparica, Portugal
[4] Instituto de Física Fundamental, Consejo Superior de Investigaciones Científicas, Serrano 113-bis, 28006 Madrid, Spain
[5] Centre for Medical Radiation Physics, University of Wollongong, 2522 NSW, Australia

Received 30 April 2013 / Received in final form 29 July 2013
Published online (Inserted Later) – © EDP Sciences, Società Italiana di Fisica, Springer-Verlag 2013

Abstract. This colloquium describes an approach to incorporate into radiation damage models the effect of low and intermediate energy (0–100 eV) electrons and positrons, slowing down in biologically relevant materials (water and representative biomolecules). The core of the modelling procedure is a C++ computing programme named "Low Energy Particle Track Simulation (LEPTS)", which is compatible with available general purpose Monte Carlo packages. Input parameters are carefully selected from theoretical and experimental cross section data and energy loss distribution functions. Data sources used for this purpose are reviewed showing examples of electron and positron cross section and energy loss data for interactions with different media of increasing complexity: atoms, molecules, clusters and condense matter. Finally, we show how such a model can be used to develop an effective dosimetric tool at the molecular level (i.e. nanodosimetry). Recent experimental developments to study the fragmentation induced in biologically material by charge transfer from neutrals and negative ions are also included.

1 Introduction

Advanced uses of radiation in radiotherapy, as ion beam cancer therapy [1,2] and targeting nanoparticles to enhance radiation effects [3,4], as well as in radiodiagnostic procedures like PET (Positron Emission Tomography) scanning, are demanding radiation interaction models at the molecular level including the effect of any generated secondary particles. At this level, low energy secondary electrons are now recognized as being the main instigator for radiation induced damage [5–8].

Traditional dosimetry for radiotherapy is based on the energy deposited by the radiation per mass unit (absorbed dose), which provides a macroscopic description of radiation effects. Some years ago, in order to increase the level of detail of this description, microdosimetry was developed by redefining radiation representative parameters, as reported in reference [9]. Although this formalism allowed one to characterise radiation effects in microvolumes, typically of the size of a living cell, microdosimetric parameters are still based on the absorbed dose. More recently, aiming to describe the effect of radiation at the nanoscale, typically the size of DNA helix segments, the concept of nanodosimetry has been introduced. A first attempt to typify radiation damage in nanovolumes was carried out by Grosswendt [10], by proposing the size of ionization cluster distribution in a nanovolume, of about 50 nm^3, as an indicator of the induced damage to DNA. This is clearly a better approach to characterise radiation damage at the molecular level, than simply the energy deposition, but it only accounts for damage produced by ionizing particles. No dissociations induced by electronic and vibrational excitations of the molecule or electron attachment are included and, as mentioned above, these low energy processes are the most efficient to produce bond-breaking in biomolecular systems. Therefore, further information about induced fragmentation patterns is required to evaluate radiation damage at the nanoscale. In addition, no equilibrium about energy deposition can be assumed in these nanovolumes as they are usually placed in low dose penumbra and boundary regions where conventional dosimetry is not applicable. Transport of secondary species from high-dose irradiated areas thus needs to be precisely simulated, so that accurate energy and angular distribution functions for those species interacting with the medium are required.

On the other hand, positrons have become important subjects to study as their interactions with biomolecular

[a] e-mail: g.garcia@iff.csic.es

systems are the basis of positron emission tomography (PET scanning). Attaching positron emitters to appropriate molecular tracers and mapping positron annihilation concentrations in the target is currently one of the most powerful tools to detect early tumour activities or predicting some brain diseases such as Alzheimer. More recently, PET techniques have also been used as a complement of ion beam cancer treatments for dosimetry purposes. In particular the passage of fast ions through biological material activates positron emitters (^{11}C, ^{15}O), which can be used as indicators for radiation dosimetry by employing PET imaging techniques.

Finally, another important objective of radiation models at the molecular level is to consider the role of radicals, both charged and neutral, that can generate indirect damage by charge transfer or reactive mechanisms which finally lead to structural changes in the biomolecular systems.

This article reviews the procedures we followed during the last few years in order to develop a simulation tool, based on a physical approach to the scattering and energy transfer processes which are crucial at the end of the radiation tracks, where low energy secondary species are dominant, to determine radiation damage in terms of bond breaking and induced molecular dissociations. The particular subjects of this study are electrons, positrons and radicals interacting with biologically relevant molecules (water and structural components of DNA and RNA). The effects of introducing some radiosensitizers, as nanoparticles [3,4], to enhance secondary electron generation will be also analysed, in terms of providing an approach to incorporate them into the model. Finally, our recent experimental studies on anionic fragmentation of biomolecules, by charge transfer processes, will be summarized. These give some indications of how to introduce indirect radical effects in radiation damage models at the molecular level.

2 Input data requirements and sources for electrons and positrons

Modelling single electron and positron tracks in biologically relevant media requires an important amount of scattering data, in terms of cross section and energy loss. The structure of the tracks is defined by a combination of integral and differential scattering cross sections together with the energy transferred in the single scattering events. These data would be needed for a wide energy range from almost zero (thermal energies) up to the high energy of the primary beam radiation, typically in the domain of the MeVs for applications in radiotherapy. Fortunately, biomolecular media are mainly constituted by relatively light atoms (H, C, N, O) for which electron and positron scattering can be accurately described, even for elastic processes [11–13], in terms of the first Born approximation [14,15] for incident energies above 10 keV. For these energies, all the required scattering information can be derived from the corresponding Bethe surfaces [15]. For this reason, we will focus our experimental and theoretical procedures to derive scattering cross section and energy loss data for electrons and positrons interacting with water and other biologically relevant molecules (tetrahydrofuran-THF, pyrimidine, DNA and RNA bases) for incident energies below 10 keV.

2.1 Electron and positron scattering cross section calculations

Electron scattering cross sections from molecular targets have been calculated for several decades, by using different methods with different degrees of sophistication when representing the target properties. Ab initio methods, based on a quantum description of the molecular target states followed by a dynamical study of the scattering equations including correlation and other effects, depending on the actual approach, can be considered the most accurate. Amongst them the R-matrix approach [16,17], symmetry-adapted single-centre expansion [18], and Schwinger multichannel procedures [19], can be highlighted. Each method has its particular limitations for the covered energy range, and type or size of target to be treated, with an update of the most representative techniques being found in reference [20]. In this context we clearly found that a general approach covering reasonably well a broad energy range and able to link with some of these previously mentioned methods, where they are applicable, needs to be developed for modelling purposes. The procedure we are proposing here is based on an independent atom representation of the molecule [21]. Consequently, only when the incident energy is high enough, to ensure that the scattering cross sections for a given atom do not interfere with those of the surrounding atoms, can we consider this approach as valid. This validity limit depends on the atoms constituting the target but in general, for those considered here, we can assume that for energies above 100 eV the independent atom model (IAM) is a good approximation (see comparison with experiments for different molecules in [22]). For lower energies, we proposed a simple procedure based on the calculation of the overlap of the atomic cross sections according to their positions in the molecule. Sequential details on the calculation method we developed, to obtain electron and positron scattering cross sections from atoms, molecules, clusters and condensed matter, over a broad energy range, typically 30–10 000 eV, will be given in the next subsections. Note that our calculation is averaged over all incident angles and therefore effects depending on the direction of approach of the incoming projectile are not considered.

2.1.1 Cross section calculations for electron and positron scattering from atoms

The first step to develop a general scattering calculation framework for electrons and positrons, based on independent atom representations, is to describe interactions with atomic targets as accurately as possible (within the limitation imposed by the considered energy range). For

this purpose, we represent scattering from atoms by an interacting complex potential (i.e. the optical potential):

$$V_{\rm opt}(r) = V(r) + iV^a(r) \quad (1)$$

whose real part, $V(r)$, accounts for the elastic scattering of the incident electrons/positrons, while the imaginary part, $V^a(r)$, represents the inelastic processes that are considered as "absorptions" from the incident beam.

For electron scattering, to construct this complex potential for each atom, the real part of the potential is represented by the sum of three terms: (i) a static term derived from a Hartree-Fock calculation of the atomic charge distribution [23], (ii) an exchange term to account for the indistinguishability of the incident and target electrons [24] and (iii) a polarisation term [25] for the long-range interactions which depend on the target dipole polarisability [26]. The imaginary part, following the procedure of Staszewska et al. [27], then treats inelastic scattering as electron-electron collisions. However we initially found some major discrepancies in the available scattering data, which were subsequently corrected when a physical formulation of the absorption potential [28,29] was introduced. Further improvements to the original formulation, such as the inclusion of screening effects, local velocity corrections and in the description of the electrons' indistinguishability [30], finally led to a model that provides a good approximation of electron-atom scattering over a broad energy range [22,31]. An excellent recent example of this was for elastic electron-atomic iodine scattering [32], where the optical potential results compared very favourably with those from a highly sophisticated Dirac-B-spline R-matrix computation.

Concerning positron scattering from atoms, we used an adapted version of the above optical potential. Now, the real part has only two terms: (i) a static potential derived from a standard Hartree–Fock calculation of the atomic charge density, following a similar procedure to that proposed by Reid and Wadhera [33–35]; and (ii) the polarization potential. As exchange does not apply in this case, low energy positron elastic scattering cross sections generally tend to be lower in value compared to those for the corresponding electron scattering cases. Concerning the polarisation term, initial calculations from Zhang et al. [36] used a simple asymptotic expression proportional to the target polarisabilty but introducing a corrective parameter for short distances. However, as this term gives the only attractive contribution to the positron scattering calculations, it becomes relatively more relevant than for electron scattering. For this reason we have derived a new polarisation potential based on that proposed by McEachran et al. [37] for noble gases, by scaling with a constant parameter to diffuse the charge density of each target orbital which in turn leads to the appropriate dipole polarisability for the target (see Ref. [38] for details). For the imaginary part, i.e. the absorption potential which accounts for the inelastic processes, we used initially the scheme proposed in references [33–35], based on Staszewska's procedure [27] for electron scattering, which considers inelastic processes as binary collisions between the incident particles and a "quasi-free" electron cloud representing the target electrons. The most controversial part of this potential is the procedure to define the threshold energy (Δ), in order to initiate the absorption process (see Blanco and García [28–30] for details). As far as the inelastic cross sections are concerned, the main difference between electron and positron scattering is the positronium formation channel. Consistent with the foundations of our approach, the threshold energy (Δ) should be the energy of the first excited level. For electron-atom scattering it should thus be the energy of the lowest excited electronic state (E_{res}). However, around this threshold energy, an important limitation of this method may arise for positrons. Indeed, at these energies, positronium formation is a dominant inelastic channel which cannot be explained in terms of binary collisions [39], and therefore was not included in the original formulation of the absorption potential. The threshold for positronium formation (Δ_p) is 6.8 eV below the ionisation limit of all the species in question, which normally results in an energy which is less than that for the first discrete excited level. For this reason, Reid and Wadehra [33–35] proposed to use the threshold energy for positronium formation as the absorption threshold parameter ($\Delta = \Delta_p$) (i.e. a semi-empirical approach). This procedure was initially considered as an indirect way of introducing positronium formation into the absorption potential, and indeed some agreement with the then available experimental data was found for the noble gases. However, as we have recently noticed in argon [38], it is an experimentally evident fact that positronium formation actually occurs over a relatively narrow energy range, namely from threshold up to about 100 eV. Contrary to this, the effect produced by lowering the absorption potential threshold extends over the whole energy range. This means that by simply lowering the absorption threshold we are probably overestimating the total cross section at the higher energies. In fact, positronium formation at these energies can be considered as a doubly-binary collision process. Apart from the binary collision with a target electron, which can be accounted for the original absorption potential, it requires an additional positron or electron scattering off the residual ion [39]. This situation makes it difficult to introduce positronium formation as an independent inelastic process. By taking these considerations into account we proposed to adopt a compromise solution, by defining an energy-dependent parameter for the absorption threshold [40]:

$$\Delta\,(E) = \Delta_e - (\Delta_e - \Delta_p)e^{-\left(\frac{E-\Delta_p}{E_m}\right)}, \quad (2)$$

where Δ_e is the lowest excitation energy of the atomic targets, Δ_p is the Ps formation threshold and E_m is a characteristic energy at which the inelastic cross section, without positronium formation, reaches its maximum (generally placed in $E_m = 20$ eV [40]). This expression provides values between the limit conditions: $\Delta(E) = \Delta_p$ for energies close to the Ps formation threshold and $\Delta(E) = \Delta_e$ for higher energies. A smooth transition between both limits is modulated by the negative exponential and governed by the E_m parameter [40].

2.1.2 Cross section calculations for electron and positron scattering from molecules

In order to obtain molecular cross sections, the independent atom model (IAM) has been followed by applying a coherent addition procedure, commonly known as the additivity rule (AR). In this approach, the molecular scattering amplitude ($F(\theta)$) is derived from the sum of the above atomic amplitudes which lead to the differential elastic cross section for the molecule ($d\sigma^{molec}/d\Omega$), according to

$$F(\theta) = \sum_{atoms} f_i(\theta) e^{iq.r_i};$$
$$\frac{d\sigma_{el}^{molecule}}{d\Omega} = \sum_{i,j} f_i(\theta) f_j^*(\theta) \frac{\sin qr_{ij}}{q} r_{ij}, \qquad (3)$$

where q is the momentum transferred in the scattering process and r_{ij} is the distance between the ith and jth atoms.

Integral elastic cross sections for the molecule can then be determined by integrating equation (1). Alternatively, elastic cross sections can be derived from the atomic scattering amplitudes in conjunction with the optical theorem [30] giving:

$$\sigma_{el}^{molecule} = \sum_{atoms} \sigma_{el}^{atom}. \qquad (4)$$

Unfortunately, in its original form, we found an inherent contradiction between the integral cross section derived from those two approaches, which suggested that the optical theorem was being violated [41]. This, however, was resolved using a normalisation technique so that integral cross sections determined from the two methods are now entirely consistent.

The main limitation of the AR is that no molecular structure is considered, thus it is really only applicable when the incident electrons are fast enough to effectively "see" the target molecule as a sum of the individual atoms (typically above ∼100 eV). To reduce this limitation we developed the SCAR method [22,31], which considers the geometry of the corresponding molecule (atomic positions and bond lengths) by introducing some screening coefficients which modify both the differential and integral cross sections, especially for lower energies [22,31],

$$\sigma^{elast} = \sum_i s_i \sigma_i^{elast} \qquad (5)$$

where s_i are the screening coefficients which account for the geometrical overlapping of the atoms. Their values are within the range $0 \leqslant s_i \leqslant 1$, so that they reduce the contribution from each atom to the total cross section. To generate these coefficients is required only data on the position and the total cross section σ_i of each atom in the molecule,

$$s_i = 1 - \frac{\varepsilon_i^{(2)}}{2!} + \frac{\varepsilon_i^{(3)}}{3!} - \frac{\varepsilon_i^{(4)}}{4!} + \ldots \pm \frac{\varepsilon_i^{(N)}}{N!}, \qquad (6)$$

$$\varepsilon_i^{(k)} \cong \frac{N-k+1}{N-1} \sum_{j(\neq i)} \frac{\sigma_j \varepsilon_j^{(k-1)}}{\alpha_{ij}} \, (k = 2, \ldots, N) \qquad (7)$$

where N accounts for the number of atoms in the target molecule, the j index runs over all the N atoms, except the atom i, and $\alpha_{ij} = \max(4\pi r_{ij}^2, \sigma_i, \sigma_j)$ being r_{ij} the distance between the atoms i and j (a detailed discussion is given in [22,31]).

With this correction the range of validity of the IAM-SCAR method might be extended down to about 30 eV. For intermediate and high energies (30–10 000 eV) our approach has been proven to be a powerful tool to calculate electron scattering cross sections from a high variety of molecules of very different sizes, from diatomic to complex biomolecules [31,42]. For positron scattering, however, further studies are needed in order to establish the lower energy limit of the IAM-SCAR method.

From the above description of the IAM-SCAR procedure, it is obvious that vibrational and rotational excitations are not considered in this calculation. However, for polar molecules additional dipole-induced excitation cross sections can be calculated following the procedure suggested by Jain [43]. Basically it calculates differential and integral rotational excitation cross sections for a free electric dipole in the framework of the first Born approximation (FBA) which can be incorporated into our IAM-SCAR calculation in an incoherent way by just adding the results as an independent channel. Although rotational excitation energies are, in general, very small (typically a few meV) in comparison with the incident electron energies, in order to validate the Born approximation the latter energies should be higher than a few eVs. Under these circumstances, rotational excitation cross sections $J \rightarrow J'$ were calculated by weighting the population for the Jth rotational quantum number at 300 K and estimating the average excitation energy from the corresponding rotational constants. A unique transition starting from this J averaged state with $\Delta J = 1$ is then considered. We can label this whole procedure as the IAM-SCAR + Rotations method and it has been successfully used for polar molecules such as H_2O, pyrimidine, HCN and α-tetrahydrofurfuryl alcohol (THFA) [44–47].

Additionally, when the permanent dipole moment of the molecule in question is very large, the FBA also fails for medium and large scattering angles. In order to partially solve this, we introduced a correction based on that suggested by Dickinson [48], which brings a substantial improvement of the electron scattering cross sections for strongly polar molecules. This procedure introduces a first-order corrective term to the differential cross sections $\left(\frac{d\sigma^{Dck}}{d\Omega}\right)$, for medium and large angles but maintains the FBA result $\left(\frac{d\sigma^{B}}{d\Omega}\right)$ for the lower angles:

$$\frac{d\sigma^B}{d\Omega} \approx \frac{\mu^2}{6E_i} \frac{1}{\sin^2(\theta/2)} \qquad \theta < \theta_c, \qquad (8)$$

$$\frac{d\sigma^{Dck}}{d\Omega} \approx \frac{\pi\mu}{64E_i} \frac{1}{\sin^3(\theta/2)} \qquad \theta > \theta_c, \qquad (9)$$

where μ stands for the permanent dipole moment of the molecule and E_i the energy of the projectile. Providing that the dipole moment is larger than $\mu = 0.75$ Dy, both

curves smoothly join together at θ_c, the critical angle at which they cross each other.

2.1.3 Complementary theoretical data

The main limitation of the calculation procedure described above is its lower energy limit of applicability. For the majority of the biologically relevant molecules we have investigated, through systematic comparison with reference data, a general uncertainty of about 10% is found for both differential and integral scattering cross section data calculated with our IAM-SCAR method for energies above 30 eV. Below this limit our results provide only a qualitative indication for the correct cross section and would require some independent validation with other more sophisticated methods focussed on low energy scattering processes. We have recently demonstrated the efficacy of such complementary calculations using a single-centre expansion procedure [46] or the R-Matrix method [49]. These studies show that by combining these methods we can cover accurately, to within 10%, the energy range from nearly zero up to 10 000 eV. In addition these low energy methods provide information about resonances that can be identified as transient negative ion formations [50] which is one of the most important ways to produce molecular damage at low energies.

2.1.4 Cross section calculations for electron and positron scattering with condensed matter

Biological applications of radiation mainly treat with soft condensed matter either in the liquid or the solid state. As our modelling procedure starts from isolated atoms and molecules, it requires an additional procedure to adapt scattering data to physiological environments. In order to study the evolution of both differential and integral cross section values, when the target density increases (condensation effects), we initially calculated electron and positron cross sections for different sizes of Ar clusters (dimer, trimer, tetramer,...). Basically we followed the IAM-SCAR procedure in the same way as it is used for molecules, by considering now the cluster geometry and structure available in the literature [51]. As it will be commented in Section 3 (input data), the differential and integral cross sections are systematically modified, with respect to those of the single Ar atom, when additional atoms are aggregated into the cluster.

In order to model liquids and solids, they can be approximated as homogeneous mixtures of atoms or molecules, depending on which scattering target unit we consider, with geometrical properties determined by their temperature and density. Taking Ar as an example, and assuming that the screening corrections are not very dependent on the direction of the projectile we can apply the SCAR procedure in a similar way as we accomplished for molecules and clusters, in order to calculate the effective cross section (σ^{eff}) of an Ar atom within the liquid. A representation of the screening situation for different electron energies is shown in Figure 1. For high energy electrons (Fig. 1a), above 100 eV, where the atomic electron scattering cross sections do not overlap, an independent atom representation of the solid is appropriate. However, for intermediate energies (Fig. 1b), between 20 and 100 eV, overlap between the atomic cross sections occurs and the effective cross section of the atom i (σ_i^{eff} is less than the atomic cross section (σ_i) by the $\sigma_i j$ screening coefficients provided by the j surrounding atoms. At low energies (Fig. 1c), below 20 eV, the effective cross section approaches to the cell size $\sigma_i^{\text{eff}} = \sigma^c$ Note that as the atomic cross section (σ_I) increases, σ_i^{eff} decreases from σ_I to σ^c according to the lattice geometry. For any considered geometry we can approximate the corrective factors $s = [\sigma_i^{\text{eff}}]\sigma_I$ by the following binomial expansion:

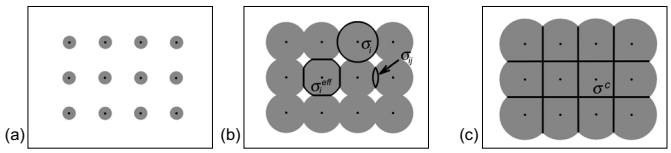

Fig. 1. Geometric representation of the Ar atomic cross sections for (a) high, (b) intermediate and (c) low incident energy electrons.

$$s = [1 + (\sigma^c/\sigma)^p]^{1/p} \tag{10}$$

where the degree of approximation to the considered geometry is given by the negative exponent p. For the situation illustrated in Figure 1, the polygonal geometry (Fig. 1b) is reached within 0.5% for $p = -21$ while the squared lattice geometry (Fig. 1c) is reproduced, within 1.5%, with $p = -8$. In practice, other intermediate geometries should be considered so an intermediate value of $p = -10$ seems to be a good compromise for this approximate treatment.

Scattering cross sections of single atoms or molecules in a liquid or solid environment are then modified, with respect to those of the isolated condition, by this environment in a selective way, strongly dependent on the energy of the incident electron or positron. This situation will be illustrated later in Section 3 with some concise examples.

Using this technique to modify electron scattering cross sections by heavy atoms (e.g., gold, gadolinium) when they are forming solid nanoparticles, provides a mechanism of introducing these radiation effect enhancers [3,4] into the present model.

2.2 Electron and positron scattering cross section measurements

It is not possible to measure all the data required by a nanoscale radiation damage model, such as that we are presenting here. This is why the scattering procedure described in the previous section is considered the main data source, dedicating the experiment to obtain reliable results for selected processes and selected energies to either validate theory or to provide information about processes out of the scope of the theoretical methods we use. Note

that no cross section data as a function of the energy transfer in the collision are provided by our calculation procedure, and therefore all the energy loss information required by the model originates from the experiment. Other relevant experimental data are the total scattering cross sections, as they can be considered as reference values, giving the sum of the integral cross sections for all the scattering processes as well as the mean free path along the particle tracks; the total and partial ionisation cross sections which, in combination with our calculated integral inelastic data, provide a reference value for the non-ionising inelastic channels (electronic excitation, neutral dissociation); and positronium formation, in the case of positrons, which provides more than the 90% of the annihilations in the medium. Remaining scattering information not entirely provided by our theoretical and experimental techniques, such as vibrational excitation and electron attachment cross sections are taken from the literature (see Ref. [52] for example). Descriptions of our experimental techniques have been published in previous publications, and therefore only a brief summary of them is required here. Additional details can be found in the main references we provide in the text that follows.

2.2.1 Total scattering cross sections

Total electron scattering cross sections (TCS), from 50 to 5000 eV, are measured with a transmission beam apparatus. The attenuation of a linear electron beam is measured as a function of the well-known target density with high angular (less than a 10^{-5} sr acceptance angle at the detector) and energy (better than 10^{-4} of the ratio of the energy spread divided by energy) resolution. We have been using this technique for years and obtaining reliable, to within 5%, electron scattering TCS for a wide variety of molecules (see Ref. [53] and references therein). As already mentioned, these TCS values are used as a reference since they represent the sum of the ICS for all the processes and so should be consistent with the values used for all the available open channels at a given energy. Below 50 eV, we variably use a compromise value between our calculated TCS and the experimental data available in the literature [52].

Concerning total positron scattering cross sections, even though technical complications arise from the need of moderating the energy of the positrons emitted by a radioactive source, and their current intensity limitations, a similar beam attenuation measurement method can be followed [39,54]. Most of the experimental TCS data for positrons we use in this modelling procedure have been obtained with a modified beam attenuation technique based on a Surko trap prototype [55]. Basically positrons emitted by a ∼50 mCi Na-22 source are slowed down with a frozen Ne moderator and cooled in a gas mixture trap via vibrational excitation of the molecules inside that gas cell. In a pulsed mode operation, under an axial confining magnetic field of 0.2 T, bunches of positrons with energy distributions around 40–6 meV are accelerated through the scattering chamber containing the molecular target in question. At the exit of the chamber the intensity of the transmitted positrons is recorded as a function of energy by means of a retarding field analyser. Details of the experimental method and set-up used can be found in reference [56].

A final validation of the electron and positron TCS data we use for a given target, is provided by their extrapolation to higher energies. According to the first Born approximation, at energies high enough to validate this approach, the TCS values are not dependent on the charge sign, and therefore they should coincide for electrons and positrons.

2.2.2 Ionisation cross sections

Electron impact ionisation cross sections are measured in a pulsed crossed beam experiment in combination with a time of flight (TOF) spectrometer to analyse the mass and charge of the generated positive ions after the collision. Details of the experimental set-up and methods to obtain absolute cross section values can be found in references [44,53]. In general, we measured directly the total ionisation cross section by using a pulsed ionisation chamber [44] and by combining those results with the mass analysis provided by the TOF spectrometer we determine the ion fragmentation pattern as a function of the incident electron energies. Ionisation cross section data are essential for modelling procedures. They are intimately linked to biological radiation damage and ionisation is the main mechanism to generate low energy electrons representing, for energies above 50 eV, about 80% of all the inelastic processes. In addition, ionic fragmentation probabilities will be required for future developments in modelling indirect damage by radicals (not implemented at the moment).

As far as positrons are concerned, ionisation processes are even more relevant for biomedical applications than they are for electrons. Apart from direct ionisation processes, similar to those occurring for electrons, positronium formation and direct annihilation processes finally lead to ionisation of the target [57]. Note that these two latter mechanisms are the basis of PET scanning applications. Direct annihilation is several orders of magnitude less probable than the previous channels, so we can consider the total ionisation cross section for positron impact as the sum of the direct ionisation and the positronium formation cross sections. As shown in reference [57], a magnetic confined positron beam apparatus similar to that described in the previous section can be used to measure selected inelastic channels: electronic excitation, positronium formation and direct ionisation. By tuning the retarding field analyser (RFA) to the energy loss range involved for the inelastic process of interest, the ratio between the corresponding inelastic cross section and the observed total cross section can be determined [58]. Until now, the experimental system described in the previous section has been devoted to the measurement of total scattering and positronium formation cross sections. For this reason, the direct ionisation cross section data we used for modelling [38] are taken from the literature and especially from

the extensive work carried out in this field by the positron group at University College London [59].

2.2.3 Electronic excitation and other inelastic channels

At intermediate energies (5–50 eV), electronic excitations provide a considerable contribution to the total inelastic cross sections. From the experimental point of view, it is not easy to obtain absolute numbers for the total electronic excitation cross sections. By using a conventional crossed beam electron scattering apparatus [60,61], with an appropriate angular and energy resolution, differential electronic excitation cross sections for selected excited states can be measured as we did in previous studies [62,63].

Other inelastic channels, such as the vibrational and rotational excitation and the electron attachment processes, become dominant at lower energies, below the electronic excitation threshold (typically below 3 eV). Available experimental data for these processes strongly depends upon the target and the energy range we are considering. In general, except for water molecules [64], they are scarce and limited to specific energies. A recent example of a critical analysis of available data, in order to get a complete cross section data set, being consistent with our experimental and theoretical data, is shown in reference [65].

For positrons, the situation with respect to these remaining inelastic channels is even worse and we usually have to take modified electron scattering data in order to complete our modelling procedure. Vibrational and rotational excitations are assumed to be the same as those corresponding to the electron case. Electronic excitations of the target are restricted to those states which do not involve spin flip, and attachment is not included.

2.3 Energy loss distribution functions

Event by event Monte Carlo modelling procedures, such as that presented here, rely on the scattering distribution probabilities derived from cross sectional data. Those determine the type of process taking place in any single scattering event, and the angular distribution of the scattered and ejected particles (incident projectile and secondary species). Another critical parameter to define the particle track structure is the energy transferred in those events. The first approach to include this parameter would be considering not only differential cross sections with respect to the scattering angle, but also differential cross sections with respect to the energy, i.e. the doubly differential cross section or even the triply differential cross section if angular and energy correlation between scattered and ejected particles is also given. Recent efforts to obtain this information for electron scattering from water and biomolecules, both theoretically and experimentally have been made [66–68]. However, these measurements are laborious if one is to cover the wide angular and energy ranges required and although the 3-body distorted wave method of calculation showed reasonable qualitative agreement with the experimental differential cross sections [68] it is not always consistent with the observed total ionisation cross sections [44]. While not ruling out the possibility of a future implementation of such a triply differential scattering model in our track simulation procedure, we decided to follow a different approach which is more convenient to our experimental and theoretical context. Basically, we use as input parameters to model the energy transferred in a scattering event the energy loss distribution functions derived from our experimental energy loss spectra. The advantage of this method is based on two pieces of important experimental evidence:

1. For high energy electrons or positrons (above 100 eV) the energy loss spectra are almost independent of the incident energy and scattering angle. For increasing energies, electrons and positrons are preferably scattered in the forward direction and the energy loss distribution between 0 and 100 eV energy loss is almost constant [52]. Only above inner shell excitation energies (285 eV for C atoms) do additional structures, about two orders of magnitude less intense, need to be included [65].
2. For low energies, say below 50 eV, the above condition does not apply and different energy loss distribution functions should be considered for different scattering angles.

Systematic studies with representative molecules connected with biological media (H_2O, CH_4, C_2H_4, THF, pyrimidine) have been carried out in three different experimental apparatus in order to cover a broad energy range from 10 to 5000 eV. The low energy electron scattering apparatus are standard crossed beam experiments located at Flinders University (Australia) and the Université de Liège (Belgium). Their energy resolution was typically within 50 to 80 meV, depending on the requirements of the measurement, and a rotatable hemispherical electrostatic spectrometer covered typically the scattering angles between 10 and 120°. For higher energies, from 50 to 50 000 eV, we used the spectrometric system placed at CSIC-Madrid, and analysed the energy of a linear electron beam passing through a pressure controlled gas cell. The angle of analysis is defined by deflecting the scattered beam with an electrostatic quadrupole covering the angular range 0–10°. Averaging measurements from both systems, for different energies and different scattering angles, we concluded that within a 20% uncertainty we can represent the electron scattering energy loss, for modelling purposes, with only two normalised distribution functions. As an example, results for CH_4 are shown in Figure 2.

In some particular cases, where details at the very end of the track are essential, additional energy loss distribution functions, for a limited energy and angular range, can be included as input data for the model with a subsequent increase of the computational task.

Other important information derived from the energy loss spectra in combination with the calculated differential elastic cross sections, are the angular distribution

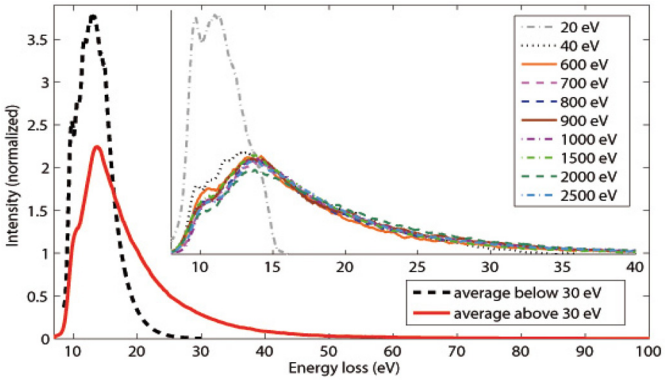

Fig. 2. Average electron energy loss distributions used for the high and low incident energy ranges. In the inset, original spectra measured in CH_4 for different energies (from 20 eV to the keV range) are compared. For 20 and 40 eV, the spectra shown are the average over all measured angles.

functions for inelastic processes. As can be seen in reference [65], by comparing the differential cross section for inelastic processes as a function of the energy transferred in the collision, with the corresponding differential cross section, we can obtain an empirical formula,

$$\frac{d^2}{\sigma(E)}d\Omega\Delta E \propto \left(\frac{d\sigma(E)}{d\Omega}\right)_{el}^{1-\Delta E/E}, \qquad (11)$$

which reproduces to a good approximation the experimental energy loss spectra as a function of the scattering angle.

For positrons we assume the same energy distribution functions as for the electrons. Few experimental energy loss spectra can be found in the literature for positrons, and even less with measurements as a function of the scattered positron angles. However as positronium formation leads to annihilation which does not affect the energy loss distributions, no important differences with the electron case can be expected.

3 Input data examples

Data requirements and the main sources from where we acquire them, which we use to model single electron and positron tracks in biologically relevant media, have been discussed in the previous section. Here we now provide some examples, on the particular cross sections and formats that we use for representative targets and particularly for water. Results for other biomolecules can be found in the references cited in the previous section.

Integral electron scattering cross sections for collisions with water molecules are shown in Figure 3. A complete analysis to derive these data has been carried out in references [44,69]. Although integral cross section data are usually plotted in a logarithmic scale (see Refs. [44,69]), here are plotted in a linear scale in order to appreciate the relative relevance of each scattering process along the energy range considered in this study.

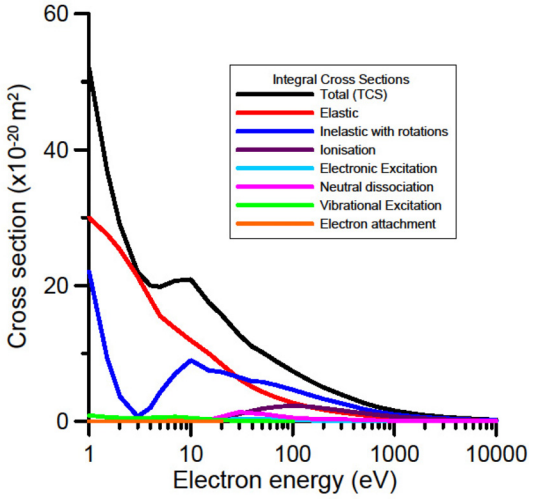

Fig. 3. Electron scattering integral cross sections for collisions with water molecules that are used as input parameters for modelling single electron tracks in water vapour. Details on data sources and the procedure followed to get a consistent set of data can be found in [69].

Total cross sections and ionisation cross sections are taken from our previous measurements, but complemented with other experimental data available in the literature. Elastic and rotational excitations are the calculated with the previously detailed procedures and the analysis of other available data in order to get a complete set of consistent data can be found in reference [69]. As discussed in [69], for energies below 5 eV, the high resolution total cross section measurements from Jones and Field [70][1] has been taken as reference values and therefore our calculated rotational excitation cross sections have been modulated in order to get consistence with those experimental values.

Angular distribution functions for elastic processes are derived from our differential elastic cross section calculation. Typical results for water molecules are shown in Figure 4, for energies ranging from 1 to 10 000 eV.

For inelastic processes, similar angular distributions are derived from equation (11). Figure 5, therefore, shows an example for a 100 eV incident energy electron and different energy loss values ranging from 0 (elastic) to 70 eV.

An example of an energy loss distribution function for high incident energies (typically above 100 eV) in water is shown in Figure 6. As described earlier, at these energies only one averaged energy loss distribution function is required. Below this energy, different energy loss distribution functions for different energy and scattering angles, according to the requirements of the modelling procedure [69], are utilised.

Input data for positrons are obtained as described in the previous section. Figure 7 shows a comparison between the total scattering cross sections for electrons and positrons in water, as calculated with the procedure described in Section 2.1. As expected, the positron and electron total scattering cross section tends to be equal

[1] And private communication.

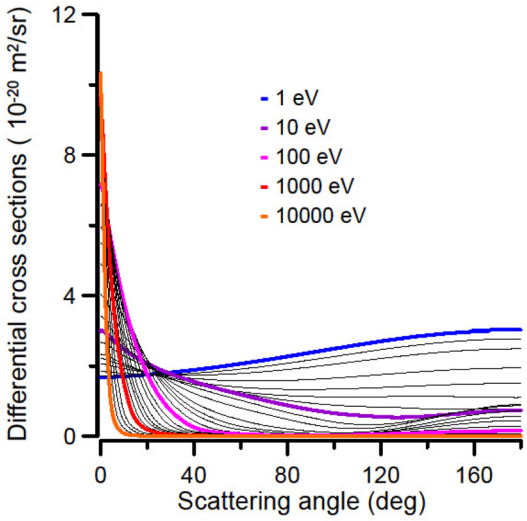

Fig. 4. Electron elastic scattering differential cross sections for collisions with water molecules, which are used to derive angular distribution functions for modelling single electron tracks in water vapour.

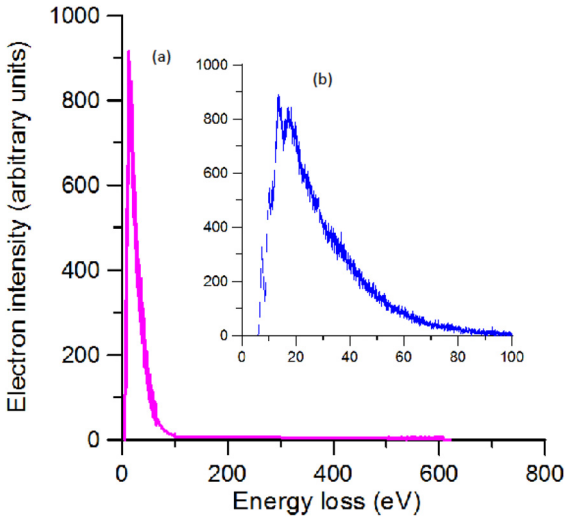

Fig. 6. A high energy (above 100 eV) electron energy loss distribution function in water, as derived from the experimental spectra. (a) Total energy loss range, (b) detail for 0–100 eV energy loss.

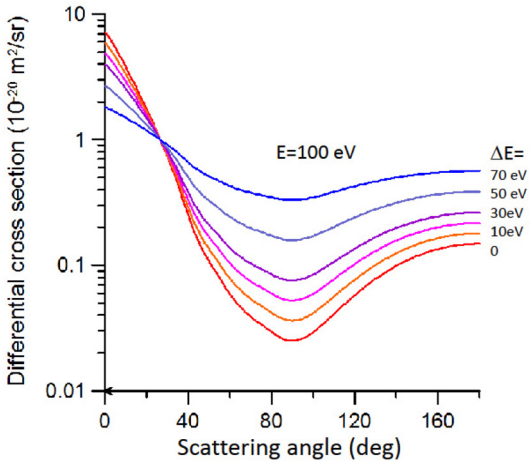

Fig. 5. Electron inelastic scattering differential cross sections for collisions with water molecules, which are used to derive angular distributions as a function of the energy loss, according to equation (11).

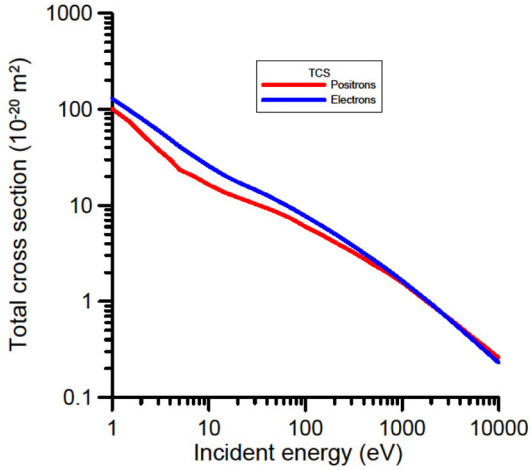

Fig. 7. Electron and positron total scattering cross sections for collisions with water molecules, as calculated with the IAM-SCAR procedure.

when the energy gets large enough. In the case of water molecules, both data merge for energies above ∼1 keV.

To illustrate how condensation effects can modify differential and integral electron scattering cross sections, elastic electron scattering differential cross sections for Ar atoms and for the dimer, trimer and tetramer Ar clusters, are plotted in Figure 8 for 1, 10 and 100 eV incident energies. As can be seen, the angular distributions of the scattered electrons are modified depending on the size of the cluster. To quantify the tendency of those condensation effects as a function of the number of atoms in the cluster, Figure 9 represents the percentage deviation of the differential electron scattering cross section of the Ar_n clusters ($n = 2, 3, 4$) with respect to that corresponding to a single Ar atom at 1 eV. As shown in this figure, some forward and backward angles are favoured by the presence of neighbouring atoms while some intermediate angles remain almost unaffected. These variations on the angular distribution of the scattering cross sections are a consequence of the coherent sum of the scattering amplitudes corresponding to the single atoms.

Similarly, the percentage deviation of the total electron scattering cross section of $Ar_n (n = 2, 3, 4)$ clusters with respect to that corresponding to isolated atoms, are plotted in Figure 10. As shown in this figure, the total cross sections always decrease when the number of atoms in the cluster increases but this effect is much more prominent for energies around 20 eV.

Applying a similar procedure to water molecules, we can transform scattering data corresponding to isolated molecules into those equivalent to molecules in a liquid

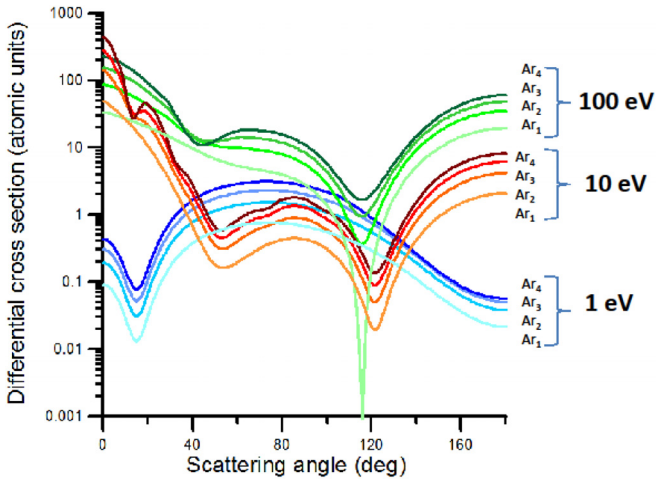

Fig. 8. Elastic electron differential scattering cross sections from Argon atoms (Ar_1) and Argon clusters (Ar_2, Ar_3, Ar_4), in atomic units (a_0^2/sr) for selected energies.

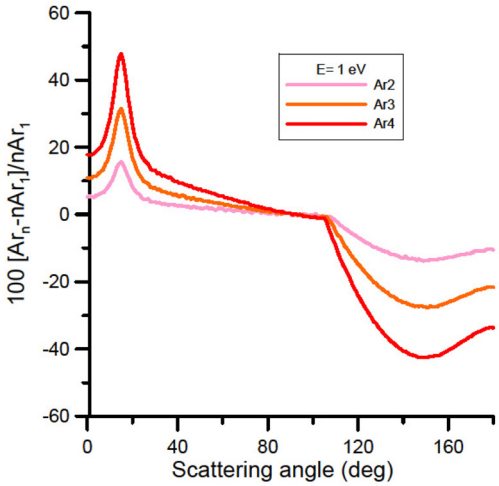

Fig. 9. Percentage deviation of the differential elastic electron scattering cross sections of Ar_n $(n = 2, 3, 4)$ clusters, with respect to the corresponding isolated atom, for 1 eV incident energy.

state. The cross sections are modified by the corrective factors calculated with the aforementioned IAM-SCAR procedure (see Sect. 2.1.4). Corresponding data for the integral, elastic and inelastic, electron scattering cross sections in liquid water are shown in Table 1. For energies below 100 eV, the cross sections tend to be larger than the intermolecular surfaces and the condensation effects start to be appreciable. Calculated corrective factors are multiplied by the corresponding molecular scattering cross section, to obtain the effective cross section of the molecule in the liquid.

This representation of the electron and positron interaction with water molecules in the liquid phase is a simple approach based exclusively in the geometry of the problem. It would be interesting to compare its predictions with other approximations available in the literature. Most of those previous studies are based on the

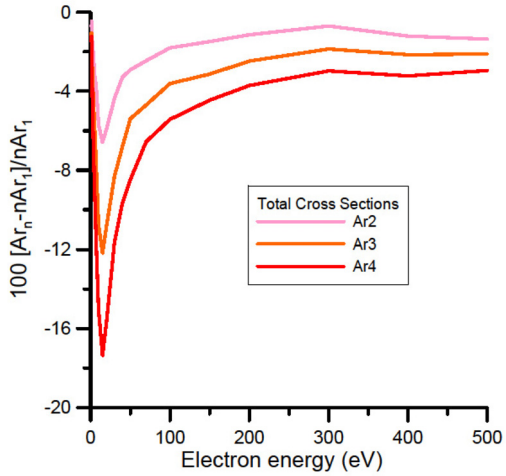

Fig. 10. Percentage deviation of the total electron scattering cross section for collisions with $Ar_n (n = 2, 3, 4)$ clusters, with respect to the corresponding to single atoms, as a function of the incident energy.

dielectric-response function, see Emfietzoglou et al. [71] for details, which relies on the calculation of a Bethe surface for liquid water [72]. Recently, Wiklund et al. [73] used this approach to derive energy loss properties and inelastic (excitation plus ionization) cross sections of electrons in liquid water. By combining these results with their calculated elastic scattering cross section and electron attachment cross section data, for the gas phase, available in the literature, they propose a cross section data set from 10 to 10 000 eV to be used for modeling purposes. Present integral elastic, inelastic and total scattering cross sections are plotted in Figure 11 together with the corresponding values of Wiklund et al. [73] for comparison. As this figure shows, total scattering cross section data are in good agreement, within 15%, for energies above 200 eV. This result seems reasonable as for energies above this limit both approximation consider that water molecules in the liquid phase behave, from the electron scattering point of view, as if they were in the gas phase. However, looking at the inelastic and elastic components, our integral inelastic cross sections are about 25% higher than those of Wiklund et al. [73] while our integral elastic values are about 20% than theirs. The discrepancy on the elastic could be justified by the simple independent atom model they use which does not consider relevant improvements we introduced in our potential [22,31] disregarding polarization and absorption effects. We have shown for rare gases that the absorption potential is always required even if only the elastic scattering is pursued. Otherwise, the calculated integral elastic cross sections are overestimated. Concerning the inelastic part, both set of data tend to converge for increasing energies. This is consistent with the fact that the dielectric function method used in [73] is based on the first Born approximation, and therefore tends to be more accurate as the incident energy increases. When energy decreases integral inelastic cross sections from [73] tend to be lower than ours, partially due to the dipole

Table 1. Theoretical integral elastic, inelastic and total scattering (TCS) cross sections (10^{-20} m^2 units) for water molecules in the gas and liquid phases, respectively, as calculated with the IAM-SCAR procedure. Corrective factors as defined in Section 2.1.4 are also given.

Energy (eV)	Gas phase			Corrective factors (s)	Liquid phase		
	Elastic	Inelastic	TCS		Elastic	Inelastic	TCS
1	30.0	98.0	128	0.0757	2.27	7.42	9.69
1.5	27.5	70.0	97.4	0.0994	2.74	6.96	9.69
2	25.3	54.9	80.1	0.121	3.06	6.64	9.69
3	21.3	38.9	60.2	0.161	3.42	6.26	9.69
4	18.0	30.5	48.5	0.200	3.59	6.10	9.69
5	15.5	25.1	40.6	0.239	3.71	5.98	9.69
7	13.5	18.7	32.2	0.301	4.08	5.64	9.69
10	11.9	13.7	25.6	0.379	4.49	5.19	9.69
15	10.0	10.1	20.1	0.483	4.82	4.86	9.69
20	8.42	8.99	17.4	0.556	4.69	5.00	9.68
30	6.22	8.37	14.6	0.664	4.13	5.56	9.67
40	5.10	7.62	12.7	0.757	3.86	5.77	9.63
50	4.37	6.94	11.3	0.840	3.67	5.83	9.50
70	3.50	5.96	9.44	0.945	3.31	5.63	8.91
100	2.74	4.96	7.70	0.990	2.71	4.91	7.63
150	2.08	3.95	6.02	0.999	2.08	3.94	6.01
200	1.71	3.33	5.04	1.0	1.71	3.33	5.04
300	1.30	2.56	3.86	1.0	1.30	2.56	3.86
400	1.07	2.10	3.19	1.0	1.072	2.11	3.19
500	0.918	1.81	2.72	1.0	0.918	1.81	2.72
700	0.722	1.41	2.13	1.0	0.722	1.41	2.13
1000	0.554	1.07	1.63	1.0	0.554	1.07	1.63
2000	0.319	0.613	0.932	1.0	0.319	0.613	0.932
3000	0.228	0.431	0.661	1.0	0.228	0.431	0.661
5000	0.146	0.275	0.420	1.0	0.145	0.275	0.420
10 000	0.0795	0.148	0.227	1.0	0.0795	0.148	0.227

induced excitation cross sections which are not considered in the calculation of Wiklund et al. [73]. Unfortunately, for lower energies, below 100 eV, where the liquid properties are expected to be dominant, no relevant conclusion can be derived from this comparison. The dielectric function method used in [73] for the inelastic part does not work at such low energies, where the Born approximation cannot be applied and, as mentioned in Section 2.1, the independent atom model they used to calculate the elastic part tend to overestimate the cross section for energies below of about 100 eV.

Another important aspect we need to consider, in order to apply our simulation procedure to the liquid phase, is the energy loss distribution function to be used. As mentioned above, for independent molecules in the gas phase, we use the energy loss distribution functions derived from our experiments. Those experiments do not run for liquids and as far as we know related data in the literature are almost inexistent, especially for the low energies where we are particularly interested here. However we can still use our energy loss distribution functions for isolated molecules after some modification, if required, via an approach based on the collisional stopping power $(-dE/dx)_{col}$, or energy loss per unit path length (x), of electrons in H_2O according to the expression [44]:

$$-\frac{1}{\rho}\left(\frac{dE}{dx}\right)_{col} = \frac{N_a}{M}\overline{E}\sigma_{inel}, \qquad (12)$$

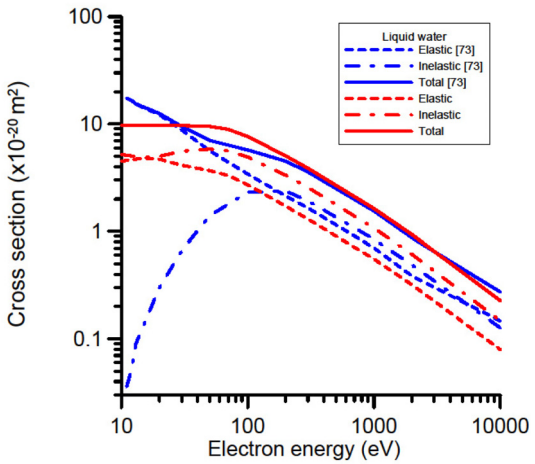

Fig. 11. Integral electron scattering cross sections in liquid water. Present work: -, total scattering cross section; -.-, integral inelastic cross section; —, integral elastic cross section. Reference [73]: -, total scattering cross section; -.-, integral inelastic cross section; —, integral elastic cross section.

where ρ is the density of the target, σ_{inel} is the integral inelastic cross section, N_a is the Avogadro constant, M the molar mass and $\bar{E}$ is the mean excitation energy derived from the experimental energy loss spectra. The stopping power of high energy particles in liquids can be calculated

with reasonable accuracy (depends on the energy of the particle) by using the properties of the dielectric function, as developed in reference [71], within the framework of the first Born approximation. In the case of water, calculated electron stopping powers for vapour and liquid water are available in the NIST databases [74] for energies above 1 keV. At these energies, the stopping powers of electrons in liquid water differ from those corresponding to water vapour by less than 2%. This difference is within the estimated error limits for our energy loss distribution function for water molecules and, given the condensation coefficient at these energies equals to 1, we can conclude that the energy loss distribution functions derived for water vapour (see Fig. 6) are also valid for liquid water. In other cases the energy loss distribution functions can be slightly shifted in energy, but maintaining their shape in order to obtain the appropriate average energy loss.

4 Monte Carlo simulations

Following the procedures described in Sections 2 and 3, we can obtain a complete set of input data for the simulation programme. For this purpose we designed a new programme with the following requirements:

1. compatible with general purpose Monte Carlo codes commonly in use for radiation dosimetry, such as GEANT4 (Geometry And Tracking4) [75] and Penelope (PENetration and Energy Loss of Positrons and Electrons) [76]. Those programmes have been proven for high energy electrons and photons. This compatibility allowed us to restrict our code development to the low energy domain, below 10 keV;
2. incorporating a flexible tool to define target composition and geometries;
3. including a powerful visual tool to be implemented in medical applications, allowing interactive output options depending on the characteristics of the problem in question.

4.1 Low energy particle track simulation (LEPTS) programme

Under these initial assumptions, we decided to base our first design on the GEANT4 tool kit developed at CERN [75]. This covers all the high energy processes and is flexible enough to allow us to incorporate all the new physics related to low energy electron and positron interactions. These new processes form the core of our low energy particle track simulation (LEPTS) code. Additionally, we incorporated other related tools such as GAMOS (GEANT4-Based Architecture for Medicine-Oriented Simulations) [77]. This combination provides a valuable set of tools related to the simulation of particle transport through matter. We use them to simulate materials, particle tracking, hit processes, build geometries, etc. A wide range of physical processes are available, so we can concentrate our effort on the interaction of low energy

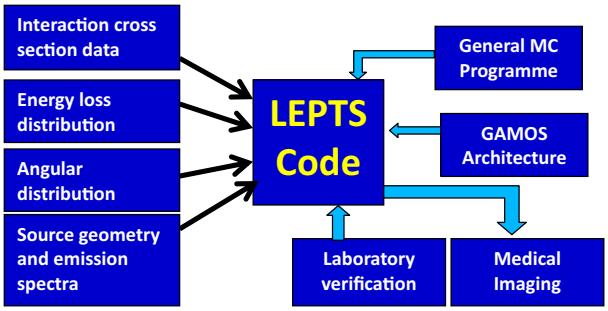

Fig. 12. Flow diagram of the modelling procedure: inputs, output and feedback.

(0–10 keV) electrons and positrons. All this new physics has been introduced by writing a new C++ code which includes all the required processes: elastic, ionisation, electronic excitation, vibro-rotational excitation, electron attachment, positronium formation, etc. using our collisional databases as input parameters (see Sect. 3). These new modules were integrated into the GAMOS' plug-in architecture and a compact set of plug-ins has been developed to account for the physics calculations, geometry, data collecting, statistics, etc. More information about the initial development of the programme as well as its technical details can be found in references [78,79].

Lately, we have developed a graphic tool (LEPTS-Visor) targeting the task of visualization and analysis of the collisional data. This tool uses the available OPENGL library to perform fast rendering of trajectories generated by the simulation code. Users can visualize the whole irradiated area or selecting regions of interest, even at the nano scale, and the option menu offers all the information related to the region of interest: energy deposited (absorbed dose), total number of interactions, number of specific processes (ionisations, dissociations, elastic events, etc.) acting as a bridge between molecular alterations and possible radiation effects.

The first biomedical applications of this model were devoted to brachytherapy, with photons emitted by I-125 seeds and electrons coming from a Ru-106 eye applicator plaque [80,81]. As shown in references [80,81], the dosimetry of the highly irradiated areas is fairly coincident using LEPTS and other dose planners but, in the lowly irradiated areas, where traditional dose planners do not assign appreciable energy deposition, low energy secondary electrons are still producing damage in terms of molecular dissociation. The main present challenge for the validation of our model is to correlate observed side-effects in medical radiation treatments with these molecular alterations induced in sensitive areas close to the irradiated tumours. A flow diagram of inputs and outputs of the LEPTS modelling procedure is shown in Figure 12. Note that verification experiments refer to preclinical trials currently in progress to systematize nanoscale predicted damage with observed biological dysfunctions.

Although the sampling procedure of our LEPTS code has been described in previous publications (see references

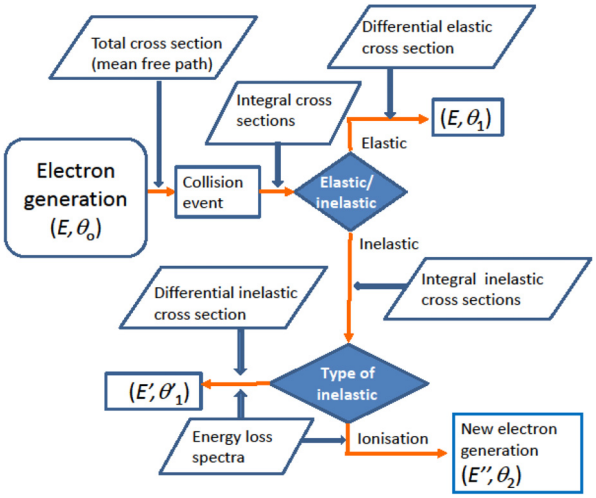

Fig. 13. Flow diagram of a single electron track simulation with the low energy particle track simulation (LEPTS) code.

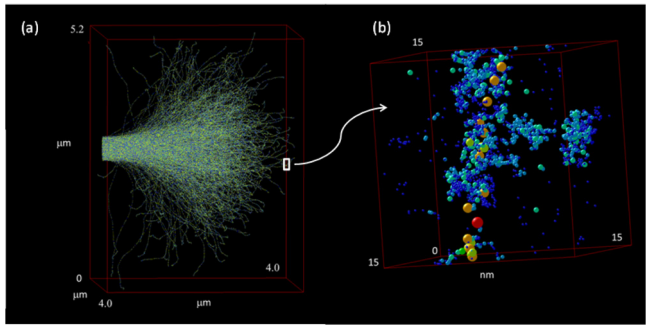

Fig. 14. An example of single electron tracks simulation in liquid water. (a) 1000 electrons with 10 keV incident energies slowing down by successive collisions (coloured balls). (b) Nanovolume detail close to the end of a selected track. The colour of the balls indicates the type of interaction: ●, elastic scattering; ●, rotational excitation; ●, vibrational excitation; ●, electronic excitation; ●, neutral dissociation; ●, ionisation; ●, electron attachment.

above) a brief summary of the entire process is given in the next paragraph.

In order to optimize the computing time consumption, the LEPTS procedure is only applied to secondary electrons with kinetic energies lower than 10 keV. In applications where the primary radiation particles are photons or high energy (>10 keV) electrons, the first step of the simulation is run with GEANT-4, but the coordinate, energy and direction of every low energy electron generated is registered in an independent file. Then, a second simulation step is carried out by using the LEPTS code for those low energy (<10 keV) electrons in the selected region of interest. The track simulation procedure of such a low energy electron is illustrated in Figure 13. Once this electron is generated with an energy ($E < 10$ keV) the Monte Carlo procedure produces a collision event by sampling the total cross section at that energy. Then, by sampling the elastic and inelastic integral cross sections, it decides whether the collision is elastic or inelastic. If it is elastic, after the collision process, the kinetic energy of the electron is almost the same as the incident (the kinetic energy transferred to the molecular target is negligible, compared to the incident energy, but it is accounted for). However, the direction of the scattered electron changes according to the angular distribution function (normalized probability as a function of the scattering angle) derived from the differential elastic cross section. If it is inelastic, the programme samples the single process integral inelastic cross sections (ionisation, excitation, attachment, etc.) to decide the type of interaction that is taking place and the energy loss distribution function (normalised probability distribution as a function of the energy loss) to evaluate the energy transferred to the molecule. For any inelastic event, the type of interaction and the energy transferred to the medium are registered. Additionally, if it is an ionisation process, a new secondary electron is generated. The energy of this secondary electron is determined by the difference between the energy transferred and the ionisation potential of the molecule while its direction is simply given by the application of the momentum conservation to the incident and the two emerging electrons.

4.2 Single electron and positron track simulation examples

In order to show the characteristics and possible applications of this modelling procedure, we have chosen some examples of electron and positron tracks in liquid water with initial energies of 10 keV. Under these conditions, single tracks for 1000 electrons until their final thermalisation are shown in Figure 14.

As can be seen in Figure 14, maximum penetration of 10 keV electrons in liquid water is less than 5 μm. All the information about energy deposition and type of interaction taking place during the thermalisation procedure is provided by the model. Both the type of interaction and the energy deposition is sorted by the simulation programme according to the probability distribution function derived from the cross sections and the energy loss distributions. At the very end of each track, when no inelastic processes are energetically available, electrons are considered thermalized after a certain number of successive elastic collisions (solvated electrons are not considered here). This information, corresponding to 10 single electron tracks, is shown in Table 2 for the whole irradiated volume and for a selected nanovolume close to the end of an electron track.

Looking at the information shown in Table 2 for the whole irradiated area, the total energy deposition corresponds to the initial electron energy, namely 10 000 eV. As for the information relative to the selected nano-volume, we can see that the energy deposition is about 372 eV, which will lead to a meaningless absorbed dose in it. However, several tens of dissociative processes in the volume are inducing damage in terms of bond breaking and structural modification of the molecules constituting the media. This is the way we define the nano-dosimetry, characterising the induced damage in terms of molecular dissociations

Table 2. Information about energy deposition and the type of interactions derived from the simulation of 10 single electron tracks of 10 keV incident energy in liquid water, both for the total irradiated volume and a selected nano-volume.

	Total irradiated area	Selected nano-volume
Volume	116 μm^3	3677 nm^3
Energy deposition	100 000 eV	371.9 eV
Number of events:		
– Elastic scattering	1 348 762	4364
– Rotational excitation	276 818	984
– Vibrational excitation	39 928	131
– Electronic excitation	390	1
– Neutral dissociation	1821	8
– Ionisation	3498	13
– Electron attachment	282	1
– Auger electrons	29	0

instead of absorbed dose. In this context, the simulation procedure described above can be considered as a useful nano-dosimetric tool for those applications which may require this level of detail.

Similar simulations can be carried out for positrons. The main differences compared to the corresponding electron tracks can be found at the end of the tracks, where low energy positrons are able to form positronium and then annihilate. In fact, the end of most of the positron tracks is positronium formation (direct annihilation, occurring only at very low energy, is a very unlikely process compared to positronium formation). Figure 15 shows the end of a positron track in water. As in the previous figure for electrons, the colour of the plotted balls represents the type of interaction (see Fig. 15). The particular case shown in this figure contains 1778 elastic collisions, 569 rotational excitations, 64 vibrational excitations, 2 neutral dissociations, 3 ionisations and 1 positronium formation which finally leads to the positron annihilation producing two 0.511 MeV photons (not shown in the picture) which escape from the medium in opposite directions.

It is difficult to estimate the accuracy of these simulated electron and positron tracks. The numerical uncertainties linked to the Monte Carlo procedures, when the number of processes used is big enough to minimize statistical fluctuations, are completely negligible with respect to the uncertainties affecting to the input parameters, i.e. cross sections and energy loss functions. Considering integrated values (elastic, inelastic and total scattering cross sections) assigned uncertainties are within 5−15% while for differential cross sections, below 30 eV these values can be increased up to 50%. In our model, differential inelastic cross sections are not related to each single process but to the energy transferred to the medium (Eq. (11)). This is a simple empirical approach but reproduces the observed energy loss spectra for different angles within 20%. Concerning positron tracks, no big differences can be expected with respect to the electron case except for those parameters for which no positron data are available and the corresponding electron data are used, i.e. vibrational

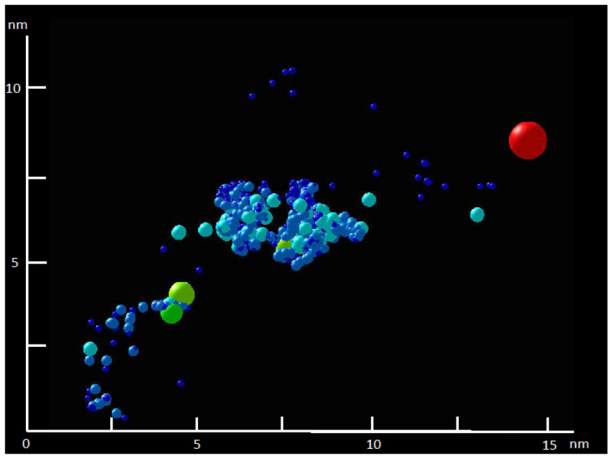

Fig. 15. Detail of the situation at the end of a single positron track in liquid water. The colour of the balls indicates the type of interaction: ●, elastic scattering; ●, rotational excitation; ●, vibrational excitation; ●, neutral dissociation; ●, ionisation; ●, positronium formation.

excitation and energy loss spectra. For energies above 10 eV, both inelastic scattering and energy loss are dominated by positronium formation, electronic excitation and ionisation. Therefore, this additional uncertainty due to the lack of positron data would be only considered for low energies, below 10 eV.

As mentioned above, this modelling procedure has been used for some medical applications [81], where the range of penetration and energy deposition of electrons in water as a function of depth are derived. This model can also be used to derive transport properties of electrons and positron, as well as positronium formation and thermalisation rates [20].

5 New capacities to implement to the model

Our modelling procedure describes, with a high level of detail, all the interaction processes related to the incident particles and the generated secondary electrons. However, the effects of other secondary species, such as charged or neutral radicals, are not considered. Positive and negative ions as well as neutral fragments can also induce important modifications to the structure and electron transfer properties of biological materials [82–84]. There are many possibilities of interaction, causing damage [85] or activating repair mechanisms [86], but we will initially focus on electron transfer processes. The effect of these processes strongly depends on the DNA component in question [82] and the subsequent reactions, leading to stabilization of the radical or producing irreversible effects, are affected by numerous factors (geometry, temperature, energy balance) which are not well understood at this moment. Our first goal will be identifying anion fragmentation induced in DNA constituents and other biomolecules, by electron transfer from other radicals including both negative ions and neutrals.

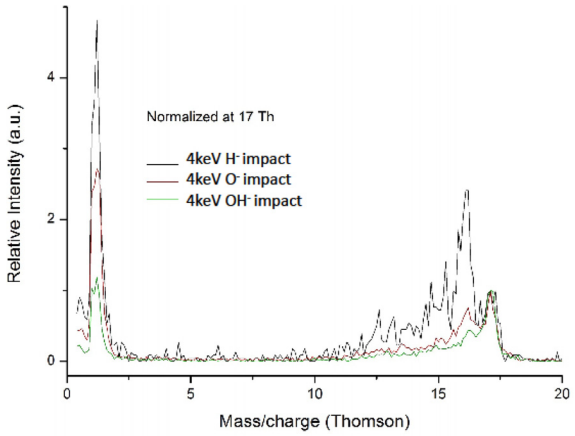

Fig. 16. Mass spectra of anions produced in 4 keV H^-, O^- and OH^- collisions with gas-phase water. The data has been normalized to each other at a mass/charge ratio of 17 Thomson (Th).

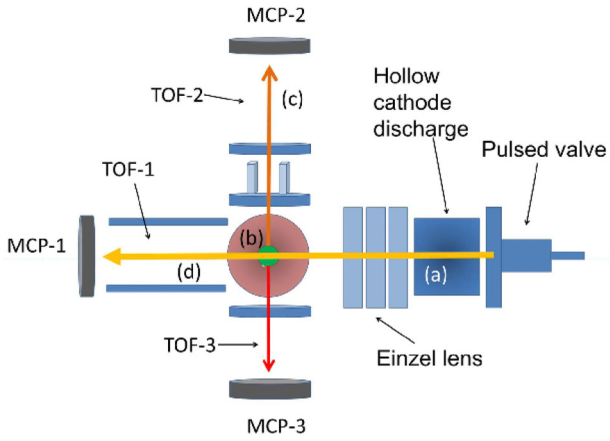

Fig. 17. Crossed beam experiment to study induced fragmentation of biomolecules by charge transfer from anionic radicals. Primary anion beam (a) is generated by a hollow cathode discharge over a supersonic beam provided by a pulsed valve. The intensity and composition of the primary beam is monitored by a time of flight spectrometer (TOF-1). This beam crosses an effusive molecular beam (b) containing the target of interest (THF, pyrimidine, DNA and RNA bases). Charged radicals produced as a consequence of the interaction are extracted through two opposite time of flight spectrometers, one for negative ions (TOF-2) and the other for positive ions (TOF-3).

5.1 Fragmentation induced by negative ion charge transfer processes

The goal of these experiments is to characterise the induced fragmentation patterns, as a function of the incident energy of the negative radical, as well as to identify the role of the neutral atom as a stabilizing third body after the electron transfer. The experimental setups are basically crossed beam experiments where anion projectiles interact with a molecular beam and the induced fragmentation is analysed by either a quadrupole mass spectrometer or a time of flight spectrometer, depending on the experimental requirements.

The first experiments were carried out for relatively high anion energy (1–4 keV). The anion beam was produced in a PS-120 Negative Ion Caesium Sputter Source and the charge-mass ratio of the produced cationic and anionic fragments were analysed with an orthogonal quadrupole mass spectrometer. Details of these measurements and results for some representative molecules (nitromethane, water, ethanol, and methanol) can be found in reference [87]. As an example, the anionic induced fragmentation by 4 keV H^-, O^- and OH^-collisions, with water molecules, is shown in Figure 16.

As shown in this figure, fragments of 1, 16 and 17 Th are identified and we assigned them to H^-, O^- and OH^-, respectively. Similar to free electron attachment, H^- formation is the dominant fragment for all the projectiles, although its yield is comparable to the other fragments, which is not in agreement with the ionic yields in free electron attachment, where H^- is one order of magnitude higher than O^- and two orders of magnitude higher than OH^- [65,88]. The yield of the most relevant fragment from the point of view of producing indirect damage, OH^-, increases notably with the mass of the projectile [87].

Similar studies for lower incident anion energies are currently in progress in our laboratory in Madrid. The experimental setup used in this case is illustrated in Figure 17. Here the ion source is a hollow cathode discharge over a pulsed molecular beam generated by a piezoelectric supersonic valve. Negative ion radicals are extracted from the cathode and accelerated onto the collision region, which is perpendicularly crossed by a molecular beam containing the target of interest. This molecular target is provided by an effusive beam generated by a temperature controlled oven. Anions induced by charge transfer are analysed in mass by a 0.92 m length TOF spectrometer. In the opposite direction, a shorter drift tube (0.52 m) analyses the mass of positive fragments produced as a consequence of the atomic collision process.

These experiments are in progress, but the incorporation into the model of fragmentation induced damage by charge transfer from charged radicals is not still available. Preliminary measurements led to promising results, and after a systematic study of different targets (THF, pyrimidine, DNA and RNA bases) and related fragmentations patterns the main indirect damage mechanisms should be able to incorporated along the track of the primary and secondary particles.

5.2 Fragmentation induced by charge transfer processes from neutral atoms

Not only can negative ions transfer electrons to surrounding molecules but so to can neutral species, provided that the local molecular electronegativity makes the process energetically accessible. Although our final objective will be neutral radicals resulting from the irradiation, in order to understand the electron transfer mechanisms and the physical parameters controlling the relative yield of

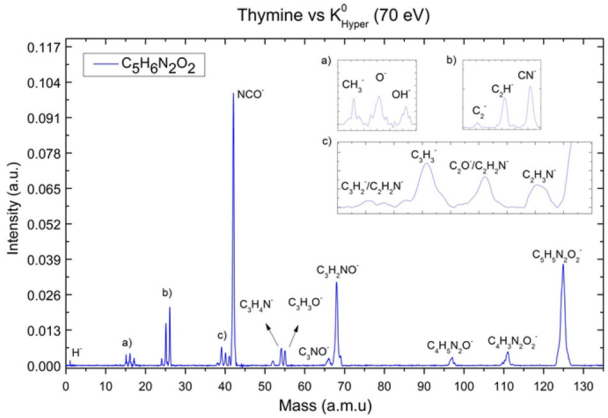

Fig. 18. Negative ion time-of-flight mass spectra for 70 eV (laboratory frame) potassium collisions with gas phase thymine. See legends on figure for further details.

the different dissociation pathways, we started the experiments by measuring the fragmentation induced from potassium atoms. This neutral atom is an excellent prototype for an electron donor projectile and can reveal important information about the bonding properties of the biomolecular systems of interest, as well as possible intramolecular electron transfer processes coupled with the electron transfer collision.

The experimental arrangement to study these collision processes is again a crossed beam configuration with a TOF mass spectrometer, but now using an energy controlled neutral potassium beam source. Experimental details can be found in references [89,90]. Just to illustrate the output from the experiment, that is used to obtain systematic patterns of induced fragmentation and relative yields, TOF mass spectra of negative fragments generated by electron transfer from potassium atoms to thymine and uracil molecules are shown in Figure 18.

In addition, dissociative electron attachment (DEA) processes leading to site-selective molecular fragmentation and the possibility of using the electron energy as a parameter to control chemical reactions have been reported [91]. We have recently shown a similar site selectivity in collisions of neutral potassium atoms with the pyrimidine bases of DNA [92]. In this case, the projectile is converted into a positive ion after the collision and the molecular target becomes a temporary negative ion allowing access to parent molecular states which are not accessible via free electron attachment experiments. These atom-molecule collision experiments, which presented as charge transfer deposited on gas-phase thymine and uracil by an electron harpooning mechanism [90], induce the loss of hydrogen which exclusively takes place from the nitrogen positions. The bond selectivity can also be made site selective by proper adjustment of the collision energy. These findings point to a new achievement in controlling chemical reactions that may have particular relevance for the investigation of early molecular processes in the nascent stages of DNA damage by secondary electrons, especially those related to strand breaks. However, we are still quite far from getting a representative data base to be included as input information for the simulation programme. Systematic charge transfer experiments from different neutral species, mainly residual radicals, colliding with electronegative DNA and RNA blocks are still required.

6 Conclusions

To study the radiation effect in biologically relevant materials, at the nanoscale level, it is indispensable to take into account the discrete nature of the radiation interaction processes. For these media, this requirement should naturally extend to the length scale of other functional units, such as macromolecules and especially DNA. Furthermore, the analysis of quantities based solely on energy deposition to the medium cannot give a complete picture of the induced radiation effects, particularly at low energies. Due to the diverse nature of the possible interactions (and their different potential for inducing molecular alterations independent on the energy they deposit), it is necessary to consider the occurrences of different collision types separately.

In this sense, we have presented a model to describe radiation interactions at the molecular level when the effect of low energy electrons or positrons is demanded by the application of interest. This model is compatible with general purpose Monte Carlo simulation tools such as GEANT4 and PENELOPE, so covering a broad energy range from the high energy of the primary radiation, typically in the order of the MeVs, down the final thermalisation of secondary particles in the order of the meVs.

The essential features of this simulation procedure are the input probability distribution functions, which are previously derived from our experimental and theoretical data, complemented with a comprehensive review of available information in the literature. We have summarised the main experimental techniques and calculation procedures we use to obtain these input data, through collaborations between the different institutions involved in this study. Our IAM-SCAR calculation procedure, including dipole rotations, has proven to be an excellent complement for the differential and integral scattering cross section measurements carried out both in beam-gas transmission and crossed beam experiments. More than ∼80% of the input information required by the model is provided within the framework of this collaboration. Remaining information, less than 20% of the whole required data, is taken from the literature. As an example, the consistency of the input data bases has been demonstrated both for electrons and positron interacting with water. Water is an excellent representative target, as it is the most abundant component of biological media and possesses common properties with other biomolecules such as a strong permanent dipole moment.

We have presented, for the first time, a procedure to apply the IAM-SCAR method to calculate corrective factors for the electron and positron scattering cross section from water molecules in the liquid phase. Although some

experimental validation is still required, this is a powerful tool to translate our single track simulation procedure from the gas phase to the condensed phase. It requires some complementary information about the energy loss distribution functions in condensed material but we have proposed a method based on the high energy electron (positron) stopping power which allows the transformation of those functions derived from the gas phase experiments.

The capability of the present model to describe radiation effects, in terms of molecular alteration (bond breaking and dissociation) in nanovolumes (nanodosimetry), has been shown and discussed by simulating electron and positron tracks slowing down in liquid water from incident energies of keVs until their final thermalisation.

Finally, state of the art of experiments to study induced fragmentation by electron transfer processes from neutral atoms and negative ions have been illustrated. The results of these experiments will ultimately constitute a new input data base to incorporate into the model, for the effect produced by neutral and anionic radicals capable of inducing damage to DNA components via electron transfer.

This work was partially supported by the Spanish Ministerio de Economía y Competitividad (Projects FIS2009-10245 and FIS2012-31230). Additional support from Portuguese Foundation for Science and Technology (FCT-MEC) through post-graduate SFRH/BD/61645/2009 and post-doctoral SFRH/BPD/68979/2010 grants as well as PEst-OE/FIS/UI0068/2011 and PTDC/FIS-ATO/1832/2012 is also noted. This work also forms part of the EU/ESF COST Action MP1002 "Nanoscale Insights into Ion Beam Cancer Therapy (Nano-IBCT)". Authors especially acknowledge the members of the Australian Research Council Centre of Excellence for Antimatter-Matter Studies (CAMS) for providing most of the experimental positron interaction cross sections used for the present modelling procedure, and, in particular, Prof S.J. Buckman, Prof M.J. Brunger, Dr J.P. Sullivan, and Prof R.P. McEachran for their constructive discussions while preparing this colloquium.

References

1. A.V. Solov'yov, E. Surdutovich, E. Scifoni, I. Mishustin, W. Greiner, Phys. Rev. E **79**, 011909 (2009)
2. M. Kanazawa, A. Kitagawa, S. Kouda, T. Nishio, M. Torikoshi, K. Noda, T. Murakami, M. Suda, T. Tomitani, T. Kanai, Y. Futami, M. Shinbo, E. Urakabe, Y. Iseki, Nucl. Phys. A **701**, 244 (2002)
3. S.J. McMahon, W.B. Hyland, M.F. Muir, J.A. Coulter, S. Jain, K.T. Butterworth, G. Schettino, G.R. Dickson, A.R. Hounsell, J.M. O'Sullivan, K.M. Prise, D.G. Hirst, F.J. Currell, Nat. Sci. Rep. **1**, 1 (2011)
4. M.S. Strano, Nat. Mater. **9**, 467 (2010)
5. B. Boudaiffa, P. Cloutier, D. Hunting, M.A. Huels, L. Sanche, Science **287**, 1658 (2000)
6. B. Bodaiffa, P. Cloutier, D. Hunting, M.A. Huels, L. Sanche, Radiat. Res. **157**, 227 (2002)
7. M.A. Huels, B. Boudaïffa, P. Cloutier, D. Hunting, L. Sanche, J. Am. Chem. Soc. **125**, 4467 (2003)
8. G. Hanel, B. Gstir, S. Denifl, P. Scheier, M. Probst, B. Farizon, M. Farizon, E. Illenberger, T.D. Märk, Phys. Rev. Lett. **90**, 188104 (2003)
9. ICRU Report 36, Microdosimetry (International Commission on Radiation Units and Measurements, Bethesda, MD, USA, 1983)
10. B. Grosswendt, Radiat. Prot. Dosimetry **110**, 789 (2004)
11. G. García, F. Manero, Phys. Rev. A **53**, 250 (1996)
12. G. García, F. Manero, Phys. Rev. A **57**, 1068 (1998)
13. F. Manero, F. Blanco, G. García, Phys. Rev. A **66**, 032713 (2002)
14. M. Inokuti, M.R.C. McDowell, J. Phys. B **7**, 2382 (1974)
15. M. Inokuti, Rev. Mod. Phys. **43**, 297 (1971)
16. A. Dora, L. Bryjko, T. van Mourik, J. Tennyson, J. Phys. B **45**, 175203 (2012)
17. Z. Mašín, J. Gorfinkiel, J. Chem. Phys. **137**, 204312 (2012)
18. A.G. Sanz, M.C. Fuss, F. Blanco, F. Sebastianelli, F.A. Gianturco, G. García, J. Chem. Phys. **137**, 124103 (2012)
19. M.A. Lima, L.M. Brescansin, A.J. da Silva, C. Winstead, V. McKoy, Phys. Rev. A **41**, 327 (1990)
20. *Radiation Damage in Biomolecular Systems*, edited by G. García Gómez-Tejedor, M.C. Fuss (Springer, London, 2012)
21. N.F. Mott, H.S.W. Massey, *The Theory of Atomic Collisions*, 3rd edn. (Clarendon Press, Oxford, 1971)
22. F. Blanco, G. García, Phys. Lett. A **317**, 458 (2003)
23. R.D. Cowan, *The Theory of Atomic Structure and Spectra* (University of California Press, London, 1981)
24. M.E. Riley, D.G. Truhlar, J. Chem. Phys. **63**, 2182 (1975)
25. X.Z. Zhang, J.F. Sun, Y.F. Liu, J. Phys. B **25**, 1893 (1992)
26. G.G. Raju, IEEE Trans. Dielectr. Electr. Insul. **16**, 1199 (2009)
27. G. Staszewska, D.W. Schwenke, D. Thirumalai, D.G. Truhlar, Phys. Rev. A **28**, 2740 (1983)
28. F. Blanco, G. García, Phys. Lett. A **255**, 147 (1999)
29. F. Blanco, G. García, Phys. Lett. A **295**, 178 (2002)
30. F. Blanco, G. García, Phys. Rev. A **67**, 022701 (2003)
31. F. Blanco, G. García, Phys. Lett. A **330**, 230 (2004)
32. O. Zatsarinny, K. Bartschat, G. García, F. Blanco, L.R. Hargreaves, D.B. Jones, R. Murrie, J.R. Brunton, M.J. Brunger, M. Hoshino, S.J. Buckman, Phys. Rev. A **83**, 042702 (2011)
33. D.D. Reid, J.M. Wadehra, Phys. Rev. A **50**, 4859 (1994)
34. D.D. Reid, J.M. Wadehra, J. Phys. B **29**, L127 (1996)
35. D.D. Reid, J.M. Wadehra, J. Phys. B **30**, 2318 (1997)
36. X. Zhang, J. Sun, Y. Liu, J. Phys. B **25**, 1893 (1992)
37. R.P. McEachran, D.L. Morgan, A.G. Ryman, A.D. Stauffer, J. Phys. B **10**, 663 (1977)
38. R.P. McEachran, J.P. Sullivan, S.J. Buckman, M.J. Brunger, M.C. Fuss, A. Muñoz, F. Blanco, R.D. White, Z. Lj Petroviæ, P. Limão-Vieira, G. García, J. Phys. B **45**, 045207 (2012)
39. M. Charlton, J.W. Humberston, *Positron Physics* (Cambridge University Press, Cambridge, 2001)
40. L. Chiari, A. Zecca, S. Giraradi, E. Trainotti, G. García, F. Blanco, R.P. McEachran, M.J. Brunger, J. Phys. B **45**, 215206 (2012)
41. J.B. Maljkoviæ, A.R. Milosavljeviæ, F. Blanco, D. Ševiæ, G. García, B.P. Marinkoviæ, Phys. Rev. A **79**, 052706 (2009)
42. F. Blanco, G. García, J. Phys. B **42**, 145203 (2009)

43. A. Jain, J. Phys. B **21**, 905 (1988)
44. A. Muñoz, J.C. Oller, F. Blanco, J.D. Gorfinkiel, P. Limão-Vieira, G. García, Phys. Rev. A **76**, 052707 (2007)
45. A. Zecca, L. Chiari, G. García, F. Blanco, E. Trainotti, M.J. Brunger, J. Phys. B **43**, 215204 (2010)
46. A.G. Sanz, M.C. Fuss, F. Blanco, F. Sebastianelli, F.A. Gianturco, G. García, J. Chem. Phys. **137**, 124103 (2012)
47. A. Zecca, L. Chiari, G. García, F. Blanco, E. Trainotti, M.J. Brunger, New J. Phys. **13**, 063019 (2011)
48. A.S. Dickinson, J. Phys. B **10**, 967 (1977)
49. A.G. Sanz, M.C. Fuss, F. Blanco, Z. Mašín, J.D. Gorfinkiel, F. Carelli, F. Sebastianelli, F.A. Gianturco, G. García, `http://dx.doi.org/10.1016/j.apradiso.2013.01.031`
50. A. García-Sanz, F. Carelli, F. Sebastianelli, F.A. Gianturco, G. García, New J. Phys. **15**, 013018 (2013)
51. B. Ulrich, A. Vredenborg, A. Malakzadeh, L. Ph. H. Schmidt, T. Havermeier, M. Meckel, K. Cole, M. Smolarski, Z. Chang, T. Jahnke, R. Dörner, J. Phys. Chem. A **115**, 6936 (2011)
52. M.C. Fuss, A. Muñoz, J.C. Oller, F. Blanco, M.-J. Hubin-Franskin, D. Almeida, P. Limão-Vieira, G. García, Chem. Phys. Lett. **486**, 110 (2010)
53. M.C. Fuss, A. Muñoz, J.C. Oller, F. Blanco, D. Almeida, P. Limão-Vieira, T.P.D. Do, M.J. Brunger, G. García, Phys. Rev. A **80**, 052709 (2009)
54. *Atomic Physics with Positrons*, edited by J.W. Humberston, E.A.G. Armour (Springer, London, 1988)
55. J.P. Sullivan, S.J. Gilbert, J.P. Marler, R.G. Greaves, S.J. Buckman, C.M. Surko, Phys. Rev. A **66**, 042708 (2002)
56. J.P. Sullivan, A. Jones, P. Caradonna, C. Makochekanwa, S.J. Buckman, Rev. Sci. Instrum. **79**, 113105 (2008)
57. J.P. Marler, C.M. Surko, Phys. Rev. A **72**, 062713 (2005)
58. A.C.L. Jones, C. Makochekanwa, P. Caradona, D.S. Slaughter, J.R. Machacek, R.P. McEachran, J.P. Sullivan, S.J. Buckman, A.D. Stauffer, I. Bray, D. Fursa, Phys. Rev. A **83**, 032701 (2011)
59. G. Laricchia, S. Armitage, D.E. Leslie, M. Szhuinska, P. Van Reeth, Rad. Phys. Chem. **68**, 21 (2003)
60. V. Vizcaino, J. Roberts, J.P. Sullivan, M.J. Brunger, S.J. Buckman, C. Winstead, V. McKoy, New J. Phys. **10**, 053002 (2008)
61. H. Kato, K. Anzai, T. Ishihara, M. Hoshino, F. Blanco, G. García, P. Limão-Vieira, M.J. Brunger, S.J. Buckman, H. Tanaka, J. Phys. B **45**, 095204 (2012)
62. T.P.T. Do, K.L. Nixon, M. Fuss, G. García, F. Blanco, M.J. Brunger, J. Chem. Phys. **136**, 184313 (2012)
63. T.P.T. Do, M. Leung, M.C. Fuss, G. García, F. Blanco, K. Ratnavelu, M.J. Brunger, J. Chem. Phys. **134**, 1443021 (2011)
64. Y. Itikawa, N. Mason, J. Phys. Chem. Ref. Data **34**, 1 (2005)
65. M.C. Fuss, A.G. Sanz, A. Muñoz, T.P.D. Do, K. Nixon, M.J. Brunger, M.-J. Hubin-Franskin, J.C. Oller, F. Blanco, G. García, Chem. Phys. Lett. **560**, 22 (2013)
66. C.J. Colyer, S.M. Bellm, B. Lohmann, G.F. Hanne, O. Al-Hagan, D.H. Madison, C.G. Ning, J. Chem. Phys. **133**, 1240302 (2010)
67. C. Champion, Phys. Med. Biol. **55**, 11 (2010)
68. J.D. Builth-Williams, S.M. Bellm, D.B. Jones, Hari Chaluvadi, D.H. Madison, C.G. Ning, B. Lohmann, M.J. Brunger, J. Chem. Phys. **136**, 024304 (2012)
69. A. Muñoz, F. Blanco, G. Garcia, P.A. Thorn, M.J. Brunger, J.P. Sullivan, S.J. Buckman, Int. J. Mass Spectrom. **277**, 175 (2008)
70. R. Èurík, J.P. Ziesel, N.C. Jones, T.A. Field, D. Field, Phys. Rev. Lett. **97**, 123202 (2006)
71. D. Emfietzoglou, K. Karava, G. Papamichael, M. Moscovitch, Phys. Med. Biol. **48**, 2355 (2003)
72. M. Dingfelder, M. Inokuti, Radiat. Environ. Biophys. **38**, 93 (1999)
73. K. Wiklund, J.M. Fernández-Varea, B.K. Lind, Phys. Med. Biol. **56**, 1985 (2011)
74. M.J. Berger, J. Coursey, M. Zucker, J. Chang, Technical Report NISTIR 4999 (National Institute of Standards and Technology, 2009), `http://www.nist.gov/pml/data/star/index.cfm`
75. S. Agostinelli et al., Nucl. Instrum. Methods A **506**, 250 (2003)
76. J. Sempau, E. Acosta, J. Baró, J.M. Fernández-Varea, F. Salvat, Nucl. Instrum. Meth. B **132**, 377 (1997)
77. M. Cañadas, P. Arce, P. Rato Mendes, Phys. Med. Biol. **56**, 273 (2011)
78. A. Roldán, J.M. Pérez, F. Blanco, A. Williart, G. García, J. Appl. Phys. **95**, 5865 (2004)
79. A. Muñoz, J.M. Pérez, G. García, F. Blanco, Nucl. Instrum. Meth. A **536**, 176 (2005)
80. M.C. Fuss, A. Muñoz, J.C. Oller, F. Blanco, P. Limão-Vieira, A. Williart, C. Huerga, M. Téllez, G. García, Eur. Phys. J. D **60**, 203 (2010)
81. M.C. Fuss, A. Muñoz, J.C. Oller, F. Blanco, A. Williart, P. Limão-Vieira, M.J.G. Borge, O. Tengblad, C. Huerga, M. Téllez, G. García, Appl. Rad. Isot. **69**, 1198 (2011)
82. S. Steenken, Biol. Chem. **378**, 1293 (1997)
83. S.O. Kelley, J.K. Barton, Science **283**, 375 (1999)
84. M. Ratner, Nature **397**, 480 (1999)
85. M. Dizdaroglu, P. Jaruga, Free Rad. Res. **46**, 382 (2012)
86. S.D. Bruner, D.P.G. Norman, G.L. Verdine, Nature **403**, 859 (2000)
87. D. Almeida, R. Antunes, G. Martins, G. Garcia, R.W. McCullough, S. Eden, P. Limão-Vieira, Int. J. Mass Spectrom. **311**, 7 (2012)
88. J. Fedor, P. Cicman, B. Coupier, S. Feil, M. Winkler, K. Gluch, J. Husarik, D. Jaksch, B. Farizon, N.J. Mason, P. Scheier, T.D. Mark, J. Phys. B **39**, 3935 (2006)
89. D. Almeida, R. Antunes, G. Martins, S. Eden, F. Ferreira da Silva, Y. Nunes, G. Garcia, P. Limão-Vieira, Phys. Chem. Chem. Phys. **13**, 15657 (2011)
90. F. Ferreira da Silva, D. Almeida, R. Antunes, G. Martins, Y. Nunes, S. Eden, G. Garcia, P. Limão-Vieira, Phys. Chem. Chem. Phys. **13**, 21621 (2011)
91. R. Balog, E. Illenberger, Phys. Rev. Lett. **91**, 213201 (2003)
92. D. Almeida, F. Ferreira da Silva, G. García, P. Limão-Vieira, Phys. Rev. Lett. **110**, 023201 (2013)